Journal Name

ARTICLE TYPE

Cite this: DOI: 00.0000/xxxxxxxxxx

Room temperature single electron transistor based on a size-selected aluminium cluster†

Vyacheslav S. Zharinov,*[a] Thomas Picot,[a] Jeroen E. Scheerder,[a] Ewald Janssens*[a] and Joris Van de Vondel*[a]

Received Date
Accepted Date

DOI: 00.0000/xxxxxxxxxx

Single electron transistors (SET) are powerful devices to study the properties of nanoscale objects. However, the capabilities to place a nano-object between electrical contacts under pristine conditions are lacking. Here, we developed a versatile two point contacting approach that tackles this challenge, which is demonstrated by constructing in-situ a prototypical SET device consisting of single aluminium cluster of 66 ± 5 atoms, deposited directly in the gold nanogap using an innovative cluster beam deposition technique. The gate driven conductance measurements demonstrate Coulomb blockade oscillations at room temperature correlating with an extracted charging energy of 0.14 eV, which is five times larger than $k_B T$ at 300 K. Our work provides a model SET device platform to probe quantum features of nano-objects with high precision.

1 Introduction

Amid the trend of downscaling modern field effect transistors (FET) [1,2], single electron transistors (SET) are promising for a future generation of nanometer scale electronic switches [3,4] and sensors [5,6]. Most SET reported today can only be operated at cryogenic temperatures, which largely limits their application potential. Therefore, several attempts have been undertaken to adapt SET designs for room temperature conditions [7–10]. SET architectures are not only of interest for electronic devices but are also highly appealing for fundamental research of individual nanosize or pointlike objects. Pursuing these goals, a variety of SETs has been realized based on either single molecules [11–14], single nanoparticles [9,10,15–17] or patterned Coulomb islands [5,8].

The design of a single electron transistor requires electron tunneling between both electrical contacts and the nanoscale object. The electrical transport through the islands is controlled by an applied gate voltage. As the distance between the contact and the island is a critical parameter for tunneling, control of the initial nanometer wide separation between the electrical contacts is required. Hereto, different approaches have been used, including break junctions [18], electrodeposition [19], and electromigration (EM) [11,20,21]. EM refers to the motion of material that is driven by high current densities and is mostly the result of momentum transfer from moving charge carriers to atoms. The advantages of EM for nanofabrication are that i) it can be implemented relatively easily using a simple control algorithm; ii) it can be performed under ultra-high vacuum (UHV) conditions, avoiding undesirable contamination effects [22,23]; and iii) it is compatible with the addition of a gate electrode. Therefore, EM was reported as a reliable method for yielding stable metallic electrodes [24,25]. As a result, the formation of contacts using EM has been proven fruitful for studies of the electronic structure of individual nanoparticles and molecules [10,11,26].

The physical and chemical properties of nanoclusters, consisting of at most of a few hundreds of atoms, dramatically depend on their precise size, spatial atomic arrangements [27–29] and composition [30]. This can be explained by their increased surface-to-volume ratio and by quantum confinement effects at these reduced dimensions [31]. The size-dependent properties of nanoclusters triggered a lot of interdisciplinary research to fabricate and characterize these fascinating building blocks and led to a variety of cluster based applications in medicine [32], catalysis [33–35], plasmonics [36], memory devices based on quantum effects [37], memristive devices [38] and neuromorphic devices [39,40]. Due to their small size, nanoclusters are ideal building blocks to fabricate room temperature SET.

A great deal of activity in the field of supported nanoclusters has been done on chemically synthesized nanoclusters covered with ligands [41]. Although ligand protected clusters are convenient to handle and exhibit high stability [42,43], their chemical synthesis limits the variety of composition materials and cluster size. An alternative is to use the technique of cluster beam deposition

[a] Laboratory of Solid-State Physics and Magnetism, KU Leuven, Celestijnenlaan 200 D, box 2414, BE-3001 Leuven, Belgium. E-mail: vyacheslav.zharinov@kuleuven.be, ewald.janssens@kuleuven.be, joris.vandevondel@kuleuven.be

† Electronic Supplementary Information (ESI) available: [details of any supplementary information available should be included here]. See DOI: 00.0000/00000000.

(CBD), in which unprotected clusters are produced by physical methods like magnetron sputtering or laser ablation. The size selection is performed in the gas phase using mass filters for ions, and soft-landed on a substrate [44,45], all under UHV conditions [46]. In comparison with chemical methods, CBD is more flexible in the elemental selection, the composition [47], and the particle size.

In this article we propose to combine EM with CBD to fabricate a cluster based SET (cSET). Both EM and CBD are performed in-situ. By monitoring the current through the gap while depositing the clusters, we can detect that a single cluster bridges the contacts after which the CBD is stopped. If the cluster is weakly connected to both contacts through tunnel barriers, adding or removing a single electron, changes the electrostatic potential of the cluster and, as a result, prohibits electron transfer through the cluster. This behavior is a cornerstone of SET devices and is called the Coulomb blockade (CB). As the cluster in a cSET has an extremely low capacitance, charging by a single electron evokes CB even at room temperature and brings these devices closer to practical applications.

The successful fabrication of a cSET is presented in four parts. In Section II we demonstrate the formation of electrical contacts with the required nanometer separation by EM. In Section III, the production and size filtering of aluminum clusters is described. This particular choice of clusters, prone to oxidation, directly proves we mitigated the problems present when studying chemically reactive clusters. The procedure of electrical connection to a single cluster is discussed in Section IV. Finally in Section V, the Coulomb blockade oscillations, observed at room temperature, are discussed.

2 Nano-separated electrical contacts

The precursor structure for the electrical contacts is a bow-tie bridge fabricated using electron beam lithography on a heavily doped Si substrate covered with a thermally grown SiO_2 layer. After exposure and developing of a spincoated double MMA+PMMA (950k) resist layer, a gold film is grown by molecular beam epitaxy. No adhesion layer is used between the gold and the SiO_2 substrate. The resist mask is removed by soaking the samples in acetone and consequent rinsing in isopropanol. A scanning electron microscope (SEM) image of the resulting bow-tie structure and the used electronic read-out scheme are shown in Fig. 1a. The narrowest region has a width of about 40 nm. For gate-controlled experiments, the Au film has a thickness of 15 nm, the SiO_2 thickness is 90 nm, and the silicon substrate is employed as a gate plate.

To produce a nanogap at the narrowest point in the bow-tie structure, we use the EM technique, which is able to surpass the resolution limitations of contemporary lithography methods [11]. Hereto, we applied a novel EM protocol that was demonstrated to have a high controllability and reproducibility [48]. The successful creation of a few atom bridge between the two contacts is reflected in the quantization of the conductance [25], which is continuously monitored during EM (see Fig. 1b). After removal of these last bridging atoms, it is expected to obtain a gap of about ~ 1 nm.

An example of the measured current-bias data of a fabricated

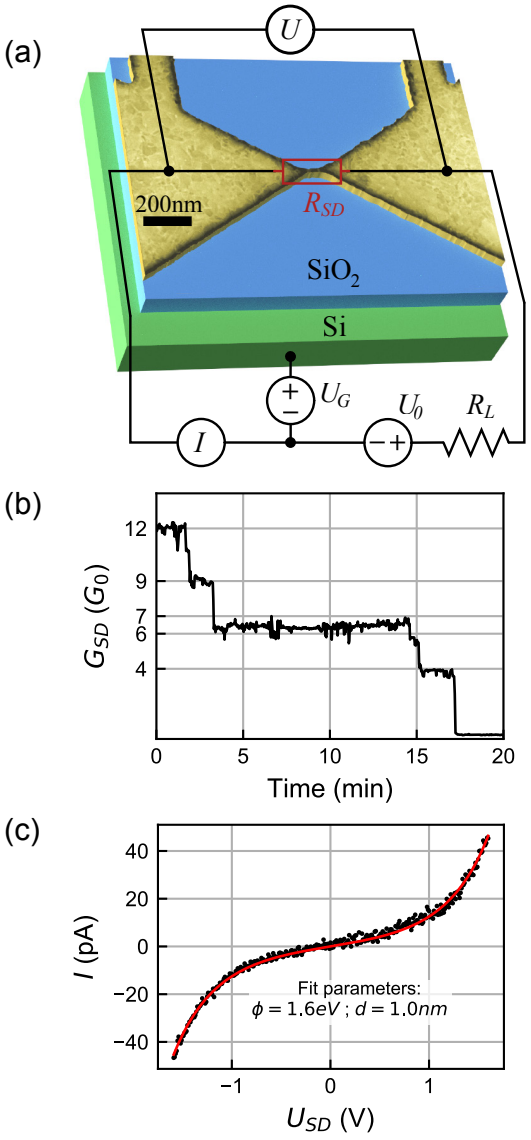

Fig. 1 (a) An illustration of a sample structure combined with a general measurement scheme. Here, the golden bow-tie bridge is tailored on the surface of the oxidized silicon wafer and the colored SEM image is rendered on top. $R_{SD} = G_{SD}^{-1}$ - junction resistance, R_L - resistance of the connecting wires, U_0 - electric bias applied to the structure, $U = U_{SD}$ and $I = I_{SD}$ - measured bias and current, respectively, and U_G - gate bias. (b) Conductance as function of time during EM. Before gap formation, G_{SD} demonstrates quantization (G_0 - quantum of conductance). (c) $I(U_{SD})$ behaviour after gap formation (black dots) and a fit of this data with Simmons formula for a barrier area of $A = 1 \times 10^{-1}\,\mathrm{nm}^2$(red curve), which demonstrates the formation of a tunnelling gap with an inter-contact barrier height $\phi \approx 1.6 \pm 0.6\,\mathrm{eV}$ and a width $d \approx 1.0 \pm 0.2\,\mathrm{nm}$.

gap is shown in Fig. 1c. The non-linear current-voltage dependence demonstrates the formation of a tunnelling gap. This data has been fitted (red line in Fig. 1c) with the Simmons model for a symmetric, rectangular, barrier modified by image forces in the intermediate voltage regime[49]. As the fitting does not critically depend on the exact barrier area[50], we fixed its value to $A = 1 \times 10^{-1}\,\mathrm{nm}^2$, which roughly corresponds to the cross-section of a single gold atom. The least squares fitting was used to find the barrier width and height, which are, respectively, $d \approx 1.0 \pm 0.2\,\mathrm{nm}$ and $\phi \approx 1.6 \pm 0.6\,\mathrm{eV}$. The error of both values is estimated by repeating the fitting procedure, while changing the barrier area by two orders of magnitude around the selected value. The received barrier height is considerably lower than the work function of gold, which is in line with expectations and with earlier reports on gold tunnelling contacts[50,51]. In addition, the obtained barrier width d should be considered as the shortest distance between the leads. Given the expected irregular geometry of the gap, clusters will have a more extended landing region to establish a weak link between the contacts.

3 Cluster production and deposition

After formation of the nanogap, clusters are deposited on the device. The different steps of clusters formation, ion guiding, mass filtering, and deposition are schematically presented in Fig. 2. Aluminium clusters are produced by plasma induced sputtering of a bulk aluminum target in a magnetron source and subsequent material condensation in an inert gas (He and Ar mixture) atmosphere (1). The formed particles with single positive charge are channelled via ion-guides (2) to a quadrupole bender (3), where residual neutral and negatively charged clusters are filtered out. More accurate mass selection is possible by the quadrupole mass filter (4). This filter enables particle selection with atomic precision for cluster sizes up to 100 atoms, but at a significant reduction of the throughput efficiency. In the current case, the resolution of the mass filter was reduced to increase the particle flux and clusters composed of 66 ± 5 atoms were selected. A mass spectrum after filtering is shown as inset in Fig. 2. Assuming the bulk density of Al and a spherical shape, the diameter of the deposited clusters is around 1.3 ± 0.1 nm (if the particles flatten to a hemisphere upon landing the diameter will be about 1.6 ± 0.1 nm). Finally, the selected cationic clusters are soft-landed (impact energy $E_{at} \approx 70$ meV per atom) on the sample through a mask (aperture Ø 1.5 mm).

Since the position of the sample holder is adjustable in three dimensions, the cluster beam can be aimed precisely at a selected device on the sample. If required, the kinetic energy of the clusters can be altered by applying an electrical bias on the sample[52]. By aiming the beam of charged particles to a metal plate connected to a picoammeter, the cluster flux can be measured, which allows to estimate the density of the deposited clusters. Overall, the cluster beam deposition approach provides a high flexibility and high control over the cluster size, the deposited amount, and the kinetic energy of the deposited clusters[45,52].

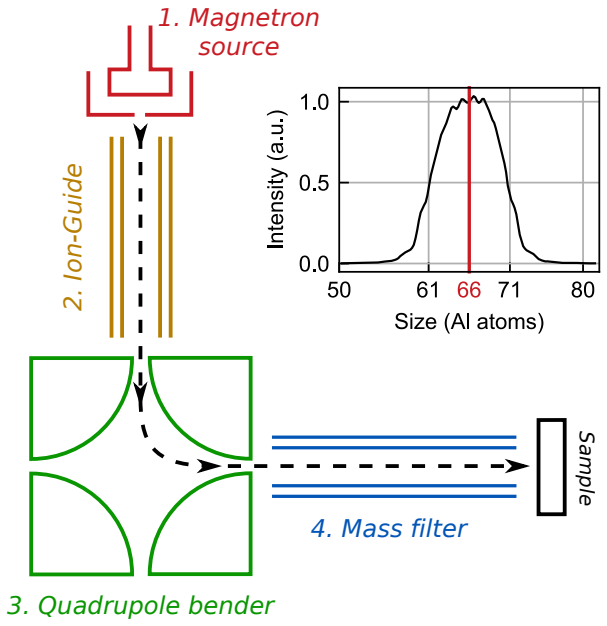

Fig. 2 Schematic overview of the cluster production, size selection, and deposition. Inset: mass spectrum of the deposited cationic aluminium clusters, filtering particles consisting of 66 ± 5 atoms.

4 Connecting to a single cluster

One of the main challenges to fabricate a single electron transistor is the difficulty to place a single molecule, quantum dot, or nanoparticle in the prefabricated gap. In earlier studies, a trial-and-error procedure is practised, which basically consist of i) making many devices, ii) measuring the devices one by one after fabrication, and iii) selecting those that show the desired single electron tunneling behavior for further characterization. The success rate, expressed as the ratio of the number of useful devices to the number of fabricated devices, of this approach is typically low[20].

We apply a more controlled strategy that allows monitoring of the electrical characteristics of the device during cluster deposition. The landing of a single cluster into the gap is directly reflected in a sudden increase of the conductance. The low deposition rate provides the required time to terminate the deposition after observing a single event. The success rate of this approach is almost 100%. A typical example of real time monitoring the conductance between the two contacts (G_{SD}), while applying a bias voltage $U_{SD} = 50\,\mathrm{mV}$, is shown in Fig. 3a. A first increase of G_{SD}, denoted as G_{dep} in Fig. 3a coincides with the start of the cluster deposition (vertical green line) and is caused by the current of charged clusters that land on the leads. A second, well defined, discontinuous increase $\Delta G_{SD} = G_{clust}$ is present at $\tau \approx 8\,\mathrm{s}$ after commencing the cluster deposition. This kind of behaviour has been observed consistently in our experiments. Rapid termination of the deposition after the jump in G_{SD} prevents that additional clusters land into the gap. Indeed, no change in G_{SD} is observed between the G_{clust} step and the end of the deposition, which implies that no additional conductive paths are created. To

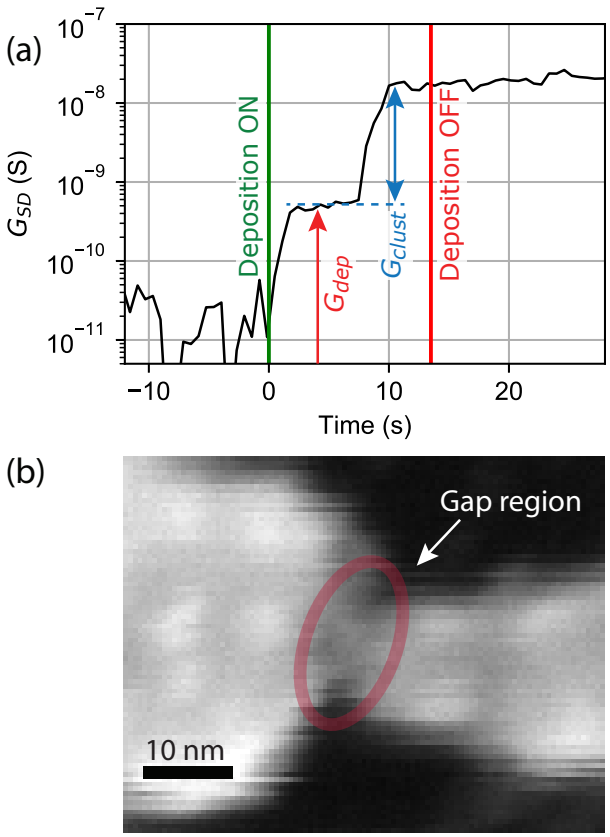

Fig. 3 (a) Conductance of the device, G_{SD}, during cluster deposition. The electric bias applied between leads is U_{SD}=50 mV. The green and red vertical lines indicate the moments that the cluster deposition starts and terminates, respectively. The red arrow points to the current of charged clusters that land on leads (G_{dep}) and thus it is no "real" increase of the conductance of the device, while the conductance jump highlighted by the blue double sided arrow denotes the connection to a single cluster (G_{clust}). (b) SEM image of a junction gap region after cluster deposition until the gap was bridged.

check the stability of the resulting system, the conductance has been monitored for nearly two hours after termination of the cluster deposition and no irreversible changes have been observed.

An SEM image of a similar device after electromigration and cluster deposition is shown in Fig. 3b. It could be concluded from this image that the used EM protocol is successful for nanogap fabrication and the aluminium clusters density around the junction is not high enough to form an interconnected percolation network. Note that the resolution of the SEM image is insufficient to distinguish the cluster inside the gap. Due to the stochastic nature of landing position/coordinates, it is not possible to calculate exactly the deposition time needed to place a cluster in the gap of an electromigrated junction. Still, one can estimate this time ($\bar{\tau}$) from the assumption that landing of a single cluster in the gap is sufficient to cause a discontinuous increase in G_{SD}. The condition can be written as $j\bar{\tau}A = 1$. Here, j is a cluster flux and if a deposited cluster center is located in the area A between leads, then the cluster bridges the contacts via two weak links. At this moment the surface particle density will be $\rho_A^* = j\bar{\tau} = 1/A \approx 0.03\,\mathrm{nm}^{-2}$. Here, $A \approx 2 \times 15$ nm^2, which length was estimated on the basis of the SEM image (Fig. 3b). This value can be compared with the one obtained using the deposition time τ until the G_{SD} jump ($\rho_A = j\tau$). For the case presented in Fig. 3a, we have $\tau \approx 8$ s and $j = 3.18 \times 10^{-3}\,\mathrm{s}^{-1}\,\mathrm{nm}^{-2}$ and thus $\rho_A \approx 0.025\,\mathrm{nm}^{-2}$, which is of the same order of magnitude as ρ_A^*. Therefore, our simple cluster connection model plausibly accords to the experimental results and indicates that the jump in G_{SD} jump is indeed caused by a single bridging cluster.

In addition, connecting to a single cluster requires staying below the percolation limit. This condition can be expressed by means of filling factor, $\eta = ja_0\tau$, that should not exceed its critical value η_c. Here, a_0 is a surface area occupied by a single deposited cluster. The ensemble of deposited clusters can be described as a two-dimensional (2D) continuum system of single size conductive circles[53,54]. Following this model, the critical filling factor is approximately 1.13. Thus, for the case presented in Fig. 3a, the time to reach the percolation threshold is $\tau_c = \eta_c/ja_0 \approx 800$ s. This is much longer than the observed deposition time until the first jump τ. Therefore, it is unlikely that the changes in G_{SD} are caused by charge percolation through a conducting path of multiple clusters. The same conclusion holds if electron tunneling is included in the percolation model. This effectively increases the diameter of the deposited clusters (increases η) and, as a result, reduces τ. The mean distance between clusters $\langle L \rangle$ at the moment of G_{clust} jump is $\langle L \rangle$=6 nm. At these distances the tunneling effects are negligibly small[49] and the impact of tunneling can be ruled out.

In order to preserve its electronic structure, a single cluster should be weakly connected to the leads by means of tunneling. Both Landauer theory for the case of elastic scattering and the Mott-Ioffe-Regel (MIR) limit of resistivity in case of inelastic scattering can help to distinguish the tunneling conductivity from the non-localized case. As follows from the MIR limit[55], it is not possible to increase the resistivity of a metal above $\rho_{IR} \approx 300\,\mu\Omega\,\mathrm{cm}$ when the carriers mean free path approaches the interatomic distance. The estimated upper resistance limit is $R_{IR} \approx 6\,\mathrm{k}\Omega$, assuming a cluster cross-section of just 1 nm^2 and a conductive line length of 4 nm (combination of the cluster diameter and of two tunneling lengths).This value is much less than the resistance through a single cluster as presented in this work (G_{clust}^{-1}=50 MΩ, Fig. 3a). G_{clust}^{-1} can neither be explained by means of Landauer ballistic transport theory with the unit transmission coefficient, as G_{clust}^{-1} greatly exceeds the quantum of resistance $R_0 = h/2e^2 \approx 13\,\mathrm{k}\Omega$. As a result, we can conclude that after landing of a cluster a tunneling contact remains. In principle, the observed G_{SD} jump can be explained by a single tunneling contact to a cluster while the second contact could be metallic. However, a working cSET requires both contacts to be weak. The presence of a Coulomb blockade effect, demonstrated in Section V, assures that both contacts are tunneling contacts.

5 Coulomb blockade

To demonstrate a working cSET, Coulomb diamonds have been measured and analysed. For this goal, a set of $I_{SD}(U_{SD})$ curves have been obtained at room temperature for different backgate

voltages, U_G. Only positive bias voltages were applied, due to the reduced lifetime of our devices for negative bias voltages caused by an increased oxide degradation. The colormap presented in Fig. 4a represent the differential conductance, $G_{SD}(U_{SD},U_G) = \partial I_{SD}(U_{SD},U_G)/\partial U_{SD}$ as a function of U_{SD} and U_G. The dashed lines contour the edges of the identified Coulomb diamonds. These results have been further analysed from the perspective of the orthodox CB model[3].

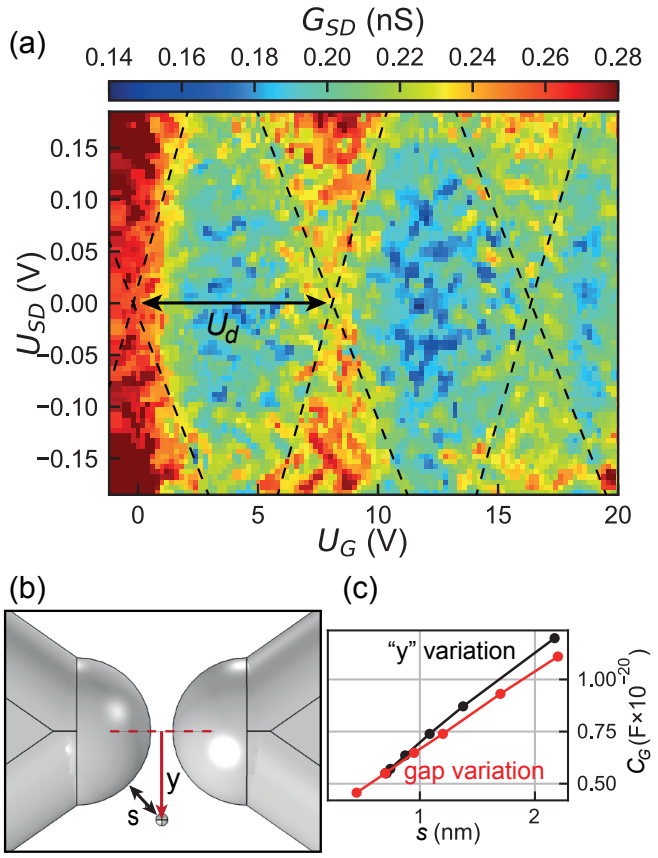

Fig. 4 (a) Example of $G_{SD}(U_{SD},U_G)$ scan map. Dashed lines indicate the borders of Coulomb diamonds. U_d is the periodicity of CB diamonds. (b) The top view of the 3D model for a cluster-gate capacitance calculation in "COMSOL Multiphysics". s- tunneling gap that is the distance between a cluster and the leads edge. Red arrow shows the "y" direction of the clucter position shift. Initial position of the cluster is exactly between the contacts. (c) Dependence of calculated C_G as a function of tunneling gap s for the case of gap size variation (red line) and the cluster position variation in the direction "y" at leads gap size 3 nm.

The height of a vertically extrapolated Coulomb diamond, $U_b \approx 0.28\,\mathrm{V}$ (not indicated in Fig. 4a), gives the total capacitance of the aluminium cluster, $C_\Sigma \approx C_\Sigma^{EX} = e/U_b = 5.8\times10^{-19}\,\mathrm{F}$, where e is an electron charge and the upper index EX means the value received from an experiment. Thus, the charging energy of the cluster (E_c) can be estimated from this value: $E_c \approx e^2/2C_\Sigma^{EX} = 0.14\,\mathrm{eV}$. This confirms that the charging energy is much larger than thermal energy at room temperature ($k_BT \approx 26\,\mathrm{meV}$), which is an obligatory condition for cSET operation. In addition, the gate-island capacitance, C_G, can be found from the relation $C_G \approx C_G^{EX} = e/U_d$, where U_d is the periodicity of the CB diamonds as a function of the backgate voltage. For the case presented in Fig. 4a, the gate-island capacitance is $C_G^{EX} = 2.0\times10^{-20}\,\mathrm{F}$. Therefore, the main contribution to the total capacitance is given by the leads and, in case we assume identical barriers, the capacitance of a single lead is $C_L^{EX} = (C_\Sigma^{EX} - C_G^{EX})/2 = 2.8\times10^{-19}\,\mathrm{F}$.

To check the validity of the experimentally obtained values, reasonable estimations regarding the capacitive coupling can be obtained from the knowledge about the cSET geometry. A straightforward method to estimate C_G is to use an analytically derived formula for a simplified system. First, the flat capacitor model has been used to estimate the lower limit of the gate-cluster capacitance $C_{Gmin} = 8\times10^{-22}\,\mathrm{F}$. Secondly, the upper limit is calculated using an approximated formula of a sphere over a conductive plane[56,57] that gives $C_{Gmax} = 3\times10^{-19}\,\mathrm{F}$ (see details in the Supplementary information). C_G^{EX} does fit in this range pointing to the consistency of the applied Coulomb diamonds model and the experiment. As the calculated C_G is spread over three orders of magnitude, a more accurate estimation approach has been also provided.

The second approach is based on the modelling of an electrostatic interaction in the cSET geometry using "COMSOL Mutliphysics" simulation package. In the result, values of gate and lead capacitances are found and are denoted as C_G^C and C_L^C respectively. The model geometry includes the cluster and the main elements of the cSET that electrostatically interact with it: leads, oxide layer and gate plate. The top view of the model is presented in Fig. 4b. It includes a semi-spherical shaped cluster of diameter d located between electrodes that have semi-spherical endings of radius $R = 10\ nm$ in accordance with the SEM image presented in Fig. 3b. To account for the local geometrical uncertainty, the tunneling distance (s) between the island and a lead has been varied by means of shifting the cluster in the direction noted in Fig. 4b as y and by variation of the gap size. In the first case the gap between the leads was fixed at 3 nm, and in the second case the cluster was located exactly between the leads ($y = 0$). The results of the calculated capacitance's C_G^C have been presented in Fig. 4c. For a realistic tunneling distance 0.4–1.5 nm, C_G^C lies in the range 0.4×10^{-20}–$0.9\times10^{-20}\,\mathrm{F}$ and only slightly depends on which of the two parameters was varied. Regardless $C_G^C < C_G^{EX}$ in the whole simulation range, the modelled values give a closer correspondence to C_G^{EX} than the capacitance limits earlier estimated from the flat and spherical capacitor models. We can reach a similar conclusion for the lead-cluster capacitance C_L^C that is calculated to be $0.9\times10^{-19}\,\mathrm{F}$ at $s\approx1\,\mathrm{nm}$. The estimated values justify the explanation of the observed G_{SD} oscillations by Coulomb blockade.

6 Conclusions

We successfully realized a SET based on a single aluminium size-selected cluster that demonstrated our new approach of making in-situ electrical contacts with nano-objects. The revealed Coulomb blockade diamonds, backed by modelling, provide a proof-of-concept. The cluster-based transistor is able to operate at room temperature, which broadens the spectrum of potential applications of clusters in integrated electronics.

The new contacting approach can further be combined with

other deposition techniques such as electrospray ionization that enables direct contact to single molecules as well. This opens prospects to study the size, structure and composition dependent electronic properties of nano-objects in a SET configuration under highly pristine conditions.

Future work includes operating those SET devices at cryogenic temperatures to increase the spectral resolution and to mechanically stabilize the system. Noteworthy, small clusters may have a substantial HOMO-LUMO gap and energy levels separation. The last one can be estimated by Kubo formula $\delta = 4E_F/3N$[58], where $E_F \approx 11.7\,\mathrm{eV}$[59] is the Fermi energy of bulk aluminium and N is the total amount of available valence electrons in the cluster (notice that every aluminium atom has three valence electrons[60]). Thus, $\delta = 79\,\mathrm{meV}$ for tested aluminium clusters. As it is more than k_BT even at room temperature, the presented cSET is potentially able to reveal energy quantization phenomena.

Conflicts of interest

There are no conflicts to declare.

Acknowledgements

This work is supported by the KU Leuven Internal Funds Project No. CREA/14/011

Notes and references

1 A. Levi, *Proceedings of the IEEE*, 2008, **96**, 335–342.

2 D. Mamaluy and X. Gao, *Applied Physics Letters*, 2015, **106**, 1–6.

3 D. Averin and K. Likharev, *Modern Problems in Condensed Matter Sciences*, Elsevier, 1991, vol. 30, pp. 173–271.

4 M. A. Kastner, *Reviews of Modern Physics*, 1992, **64**, 849–858.

5 R. J. Schoelkopf, *Science*, 1998, **280**, 1238–1242.

6 J. P. Pekola, K. P. Hirvi, J. P. Kauppinen and M. A. Paalanen, *Physical Review Letters*, 1994, **73**, 2903–2906.

7 S. J. Shin, C. S. Jung, B. J. Park, T. K. Yoon, J. J. Lee, S. J. Kim, J. B. Choi, Y. Takahashi and D. G. Hasko, *Applied Physics Letters*, 2010, **97**, 103101.

8 A. Barreiro, H. S. J. van der Zant and L. M. K. Vandersypen, *Nano Letters*, 2012, **12**, 6096–6100.

9 H. Zheng, M. Asbahi, S. Mukherjee, C. J. Mathai, K. Gangopadhyay, J. K. Yang and S. Gangopadhyay, *Nanotechnology*, 2015, **26**, year.

10 Z. Bai, X. Liu, Z. Lian, K. Zhang, G. Wang, S.-F. Shi, X. Pi and F. Song, *Chinese Physics Letters*, 2018, **35**, 037301.

11 N. Roch, S. Florens, V. Bouchiat, W. Wernsdorfer and F. Balestro, *Nature*, 2008, **453**, 633–637.

12 R. M. Metzger, A. A. Yasseri, Z. Liu, R. B. Dabke, V. Malinovskii, K.-H. Schweikart, L. Yu, H. Tiznado, F. Zaera, J. S. Lindsey, W. G. Kuhr, D. F. Bocian, J. R. Heath, M. D. Newton, D. R. Rolison, O. Sankey, K. S. Schanze, J. Yardley and X. Zhu, *Journal of Materials Chemistry*, 2008, **18**, 4364.

13 R. Vincent, S. Klyatskaya, M. Ruben, W. Wernsdorfer and F. Balestro, *Nature*, 2012, **488**, 357–360.

14 A. Cui, H. Dong and W. Hu, *Small*, 2015, **11**, 6115–6141.

15 D. C. Ralph, C. T. Black and M. Tinkham, *Physical Review Letters*, 1997, **78**, 4087–4090.

16 K. I. Bolotin, F. Kuemmeth, a. N. Pasupathy and D. C. Ralph, *Applied Physics Letters*, 2004, **84**, 3154–3156.

17 F. Kuemmeth, K. I. Bolotin, S.-F. Shi and D. C. Ralph, *Nano Letters*, 2008, **8**, 4506–4512.

18 A. R. Champagne, A. N. Pasupathy and D. C. Ralph, *Nano Letters*, 2005, **5**, 305–308.

19 Y. V. Kervennic, H. S. J. Van der Zant, A. F. Morpurgo, L. Gurevich and L. P. Kouwenhoven, *Applied Physics Letters*, 2002, **80**, 321–323.

20 H. S. J. van der Zant, Y.-V. Kervennic, M. Poot, K. O'Neill, Z. de Groot, J. M. Thijssen, H. B. Heersche, N. Stuhr-Hansen, T. Bjørnholm, D. Vanmaekelbergh, C. A. van Walree and L. W. Jenneskens, *Faraday Discuss.*, 2006, **131**, 347–356.

21 R. Hoffmann-Vogel, *Applied Physics Reviews*, 2017, **4**, 031302.

22 T. Smith, *Journal of Colloid and Interface Science*, 1980, **75**, 51–55.

23 D. P. Long, J. L. Lazorcik, B. A. Mantooth, M. H. Moore, M. A. Ratner, A. Troisi, Y. Yao, J. W. Ciszek, J. M. Tour and R. Shashidhar, *Nature Materials*, 2006, **5**, 901–908.

24 H. Park, a. K. L. Lim, a. P. Alivisatos, J. Park and P. L. McEuen, *Applied Physics Letters*, 1999, **75**, 301–303.

25 N. Ittah, I. Yutsis and Y. Selzer, *Nano Letters*, 2008, **8**, 3922–3927.

26 M. C. Hersam, *Single-Molecule Electronics*, Springer Singapore, Singapore, 2016.

27 R. Ahlrichs and S. D. Elliott, *Physical Chemistry Chemical Physics*, 1999, **1**, 13–21.

28 B. K. Rao and P. Jena, *The Journal of Chemical Physics*, 1999, **111**, 1890–1904.

29 N. Drebov and R. Ahlrichs, *The Journal of Chemical Physics*, 2010, **132**, 164703.

30 D. E. Bergeron, A. W. Castleman, T. Morisato and S. N. Khanna, *The Journal of Chemical Physics*, 2004, **121**, 10456–10466.

31 K. Sattler, *Handbook of Thin Films*, Elsevier, 2002, vol. 5, pp. 61–97.

32 E. C. Dreaden, A. M. Alkilany, X. Huang, C. J. Murphy and M. A. El-Sayed, *Chem. Soc. Rev.*, 2012, **41**, 2740–2779.

33 A. W. Castleman, *Catalysis Letters*, 2011, **141**, 1243–1253.

34 T.-W. Liao, S. Verbruggen, N. Claes, A. Yadav, D. Grandjean, S. Bals and P. Lievens, *Nanomaterials*, 2018, **8**, 30.

35 L. Geerts, S. Cosentino, T.-W. Liao, A. Yadav, P.-C. Lin, V. S. Zharinov, K.-J. Hu, A. Longo, L. M. Pereira, D. Grandjean, J. Rongé, P. Lievens and J. A. Martens, *Catalysis Today*, 2019.

36 T. Andersson, C. Zhang, M. Tchaplyguine, S. Svensson, N. Mårtensson and O. Björneholm, *Journal of Chemical Physics*, 2012, **136**, year.

37 A. Sattar, S. Fostner and S. A. Brown, *Physical Review Letters*, 2013, **111**, 136808.

38 D. B. Strukov, G. S. Snider, D. R. Stewart and R. S. Williams, *Nature*, 2008, **453**, 80–83.

39 C. Minnai, A. Bellacicca, S. A. Brown and P. Milani, *Scientific Reports*, 2017, **7**, 7955.

40 C. Louis and O. Pluchery, *Gold Nanoparticles for Physics, Chemistry and Biology*, Imperial College Press, 2012.
41 M. Walter, J. Akola, O. Lopez-Acevedo, P. D. Jadzinsky, G. Calero, C. J. Ackerson, R. L. Whetten, H. Gronbeck and H. Hakkinen, *Proceedings of the National Academy of Sciences*, 2008, **105**, 9157–9162.
42 L. A. Zotti, E. Leary, M. Soriano, J. C. Cuevas and J. J. Palacios, *Journal of the American Chemical Society*, 2013, **135**, 2052–2055.
43 L. Xu, H.-W. Liang, Y. Yang and S.-H. Yu, *Chemical Reviews*, 2018, **118**, 3209–3250.
44 V. N. Popok, I. Barke, E. E. Campbell and K.-H. Meiwes-Broer, *Surface Science Reports*, 2011, **66**, 347–377.
45 Z. Li, H.-Y. T. Chen, K. Schouteden, T. Picot, K. Houben, T.-W. Liao, C. Van Haesendonck, G. Pacchioni, P. Lievens and E. Janssens, *Nano Letters*, 2016, **16**, 3063–3070.
46 T.-W. Liao, A. Yadav, K.-J. Hu, J. van der Tol, S. Cosentino, F. D'Acapito, R. E. Palmer, C. Lenardi, R. Ferrando, D. Grandjean and P. Lievens, *Nanoscale*, 2018, **10**, 6684–6694.
47 S. Cosentino, G. Fiaschi, V. Strano, K.-j. Hu, T.-W. Liao, N. M. Hemed, A. Yadav, S. Mirabella, D. Grandjean, P. Lievens and Y. Shacham-Diamand, *The Journal of Physical Chemistry C*, 2017, **121**, 15644–15652.
48 V. S. Zharinov, X. D. A. Baumans, A. V. Silhanek, E. Janssens and J. Van de Vondel, *Review of Scientific Instruments*, 2018, **89**, 043904.
49 J. G. Simmons, *Journal of Applied Physics*, 1963, **34**, 1793–1803.
50 A. Dasgupta, M. Buret, N. Cazier, M.-M. Mennemanteuil, R. Chacon, K. Hammani, J.-C. Weeber, J. Arocas, L. Markey, G. C. des Francs, A. Uskov, I. Smetanin and A. Bouhelier, *Beilstein Journal of Nanotechnology*, 2018, **9**, 1964–1976.
51 A. Mangin, A. Anthore, M. L. Della Rocca, E. Boulat and P. Lafarge, *Physical Review B*, 2009, **80**, 235432.
52 J. E. Scheerder, T. Picot, N. Reckinger, T. Sneyder, V. S. Zharinov, J.-F. Colomer, E. Janssens and J. Van de Vondel, *Nanoscale*, 2017, **9**, 10494–10501.
53 M. Schulze, S. Gourley, S. A. Brown, A. Dunbar, J. Partridge and R. J. Blaikie, *The European Physical Journal D - Atomic, Molecular and Optical Physics*, 2003, **24**, 291–294.
54 S. Mertens and C. Moore, *Physical Review E*, 2012, **86**, 061109.
55 M. Gurvitch, *Physical Review B*, 1981, **24**, 7404–7407.
56 J. Crowley, *Proceedings of the Electrochemical Society of America Annual Meeting on Electrostatics*, 2008, Paper D1, pp 1–15.
57 S. Banerjee, S. J. McCarty and E. F. Nelsen, Proc. 2015 ESA Annu. Meeting Electrostatics, 2015.
58 R. Kubo, *Journal of the Physical Society of Japan*, 1962, **17**, 975–986.
59 N. Ashcroft and N. Mermin, *Solid state physics*, Saunders College, 1976.
60 X. Li, H. Wu, X.-B. Wang and L.-S. Wang, *Physical Review Letters*, 1998, **81**, 1909–1912.